Effect of flapping trajectories on the dragonfly aerodynamics

XU Jinliang[1], ZHAO Chuangxin[1,2], ZHANG Yongli[1] & ZHANG Yang[3]

1. Micro Energy System Laboratory, Guangzhou Institute of Energy Conversion, Chinese Academy of Sciences, Guangzhou 510640, China;
2. Graduate School of Chinese Academy of Sciences, Beijing 100039, China;
3. Department of Mechanical Engineering, Aerospace and Manufacturing Division, University of Manchester, 561000, UK

Correspondence should be addressed to Xu Jinliang (email: xujl@ms.giec.ac.cn)

Abstract The effects of translational, figure-eight and double-figure-eight flapping trajectories on the dragonfly aerodynamics were numerically studied by solving the Navier-Stokes equations. There is a common characteristic regarding the lift/drag force coefficients that the downstroke flapping provides the lift forces while the upstroke flapping creates the thrust forces for different flapping trajectories. The maximum lift force coefficient exceeds five for the translational trajectory. It is greater than six for the figure-eight and double-figure-eight flapping trajectories, which is sufficiently larger than unity under the steady state flight condition. The ellipse and double-figure-eight flapping trajectories yield the decrease of the lift force, while the figure-eight flapping trajectory yields higher lift force as well as the thrust force than the translational flapping one. During the insect flight, the wing flapping status should be changed instantaneously to satisfy various requirements. Study of the flapping trajectories on the insect aerodynamics is helpful for the design of the Micro-air-vehicles (MAVs).

Keywords: dragonfly, lift force, drag force, unsteady aerodynamics, computational fluid dynamics.

Insects cannot provide enough lift force to keep them afloat according to the conventional aerodynamics. But in fact they can not only perform the free flight, but also perform the maneuver activities such as fast take-off, suspending, back flight, etc. Detecting the insect flight secret is important for the design of the micro air vehicles (MAVs).

Early studies on the insect flight aerodynamics were focused on the experiments. The flow visualization using PIV technique[1,2] is a successful method to identify the flow field and the composition of the thrust forces, but cannot capture the details of the aerodynamics for each insect wing. The mechanical wings or airfoils were fabricated to perform the dynamic simulation measurements based on the similarity principle to obtain the instantaneous insect kinematics[3−7]. Some high lift production mechanisms, including the delayed stall (or named leading-edge vortex attachment), the pitching vortices and the trail-edge capture, are identified.

With the development of the numerical method, the computational fluid dynamics (CFD) has become an effective tool for studying the insect unsteady aerodynamics. The effect of the airfoil flow on the lift force production[8], the high lift production mechanism of the two-dimensional suspension of the dragonfly[9,10], the flight kinematics with interactions of the fore and aft wings of dragonflies[11], the unsteady flight aerodynamics of the fruit fly[12], were successfully simulated. Some high lift production mechanisms were identified through comparisons of the numerical results with the experimental measurements. Besides, the effect of the flexible wing deformation on the insect flight aerodynamics has been studied using CFD simulations in recent years[13].

The most available studies were performed with the translational trajectories of the wing flapping. However, most insects perform the flight activities with the horizontal deviation motion (not the translational flapping motion). In order to understand the effect of the horizontal deviation motion on the insect aerodynamics, we computed the lift/drag forces for several flapping trajectories (the translational, ellipse and figure-eight flapping trajectories).

Refs. [14−16] reported the detailed flapping trajectories (the ellipse, translational and figure-eight flapping motion) for the bonded or free flight insects. But they did not describe the effects of these flapping trajectories on the aerodynamics. Wang[17] suggested to give the quantitative comparisons among different flapping trajectories. Sane and Dickinson[6] used the magnetic stepping motor to control the flapping trajectories of the mechanical wing and measured the lift/drag forces for the ellipse and figure-eight flapping trajectories. But large differences exist between the measurements and the numerical simulations. They

ARTICLES

concluded that this is because the quasi-steady model cannot describe the figure-eight flapping motion. To the authors' knowledge, there are almost no studies on the effect of the different flapping trajectories on the flight aerodynamics, which is the objective of the present paper.

The insect flight aerodynamics is a complicated unsteady far field boundary external flow problem. The direct three-dimensional simulation is a challenging task[18,19]. A practical method is to simplify the three-dimensional problem as a two-dimensional one. Even though the two-dimensional simulation is unable to consider the three-dimensional effect, it saves the computational time and excludes too many parameter effects. The present paper is a two-dimensional one.

1 Description of the numerical model

Dragonfly has perfect maneuver and stable flight characteristics. Its wing flapping frequency is lower than those of other insects, but may be close to that of micro air vehicles. Thus the CFD modeling of the dragonfly flight aerodynamics can serve as the guideline for the designs of the micro air vehicles (MAVs).

Fig. 1 shows a pair of fore wings of the dragonfly. The dragonfly performs the hybrid motions: upstroke and downstroke flapping motions against its body axis and the rotation motion against the airfoil axis such as o_1o_2, i.e. changing the wing attack angles frequently. During the upstroke and downstroke motion, the two wings wiggle back and forth at a specific frequency and deviate from the Θ plane periodically. In order to simplify the computation, the three-dimensional effect is neglected due to the large wingspan to the chord ratio. We only consider the two-dimensional flight aerodynamics of the cross section in the wingspan direction, i.e. the slice chord plane (m_1m_2 plane). Strictly speaking, the wing cross section flapping plane, the m_1m_2 plane, is an arc plane with the arc center located on the wing root. For the two-dimensional computation, consider the wing motion maintained in the XOY plane with OX as the horizontal direction and OY as the vertical direction.

Fig. 2 shows the wing motion focused in the XOY plane in Fig.1. We assume that the wing cross section has the ellipse shape. The wing chord has the length two times that of the long axis of the ellipse with a thickness two times that of the short axis of the ellipse. A local coordinate xoy is established with the origin point located at the center of the wing stroke trajecto-
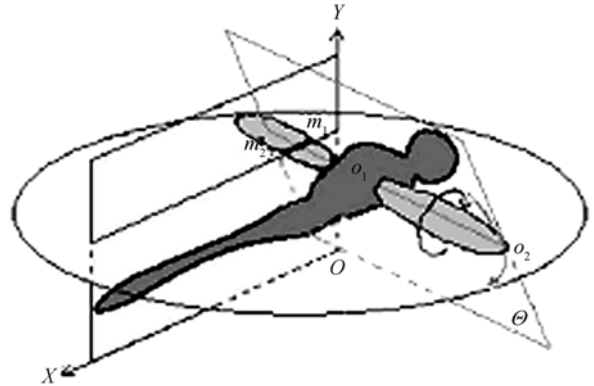

Fig. 1. Schematic diagram for the dragonfly wing motion.

ries. The x axis is in the stroke plane (Θ plane) and the y axis is perpendicular to the stroke plane Θ. For the two-dimensional computation, the wing motion consists of the translational motion along the base point and the rotation motion against the base point. The base point is in the wing rotation axis and set as the ellipse center with a distance of $0.5c$ from the leading edge of the wing. The wing motion along the x axis represents the three-dimensional upstroke and downstroke flapping. The wing motion along the y axis represents the horizontal deviation motion. The wing attack angle variation corresponds to the rotation motion. For the two-dimensional computation, the wing upstroke and downstroke flapping including the horizontal deviation motion are considered as translational motion. The variation of the wing attack angles is considered as the rotation motion. In order to consider the effect of different flapping trajectories on the flight aerodynamics, the horizontal deviation motion function is introduced in the present paper,

$$x(t) = \frac{A_0}{2}\cos(2\pi f_0 t)$$

(upstroke and downstroke motion), (1)

$$y(t) = \frac{B_0}{2}\sin(2\pi f_1 t) \text{ (horizontal deviation motion)}. (2)$$

The wing rotation motion, i.e. the variation of the attack angle of the wing, is expressed as

$$\alpha(t) = \frac{\pi}{4} - \frac{\pi}{4}\sin(2\pi f_0 t + \varphi). \tag{3}$$

The dragonfly flight parameters are set at c=1 cm, A_0=2.5 cm, f_0=40 Hz, β=$\pi/3$ for the ellipse wing based on refs. [9, 20, 21]. Besides, the wing thickness to chord ratio is normally set at h/c=0.05.
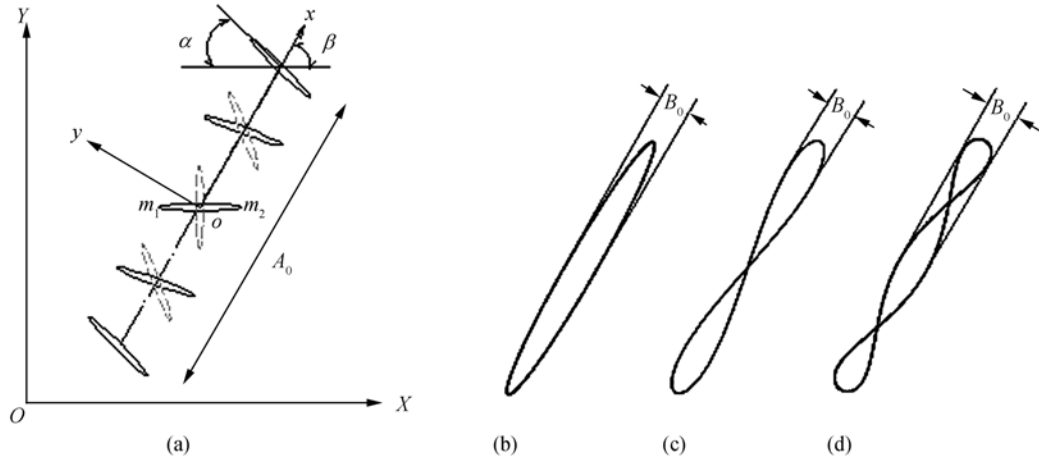
Fig. 2. (a) The wing positions at different times over a full flapping cycle for the translational flapping trajectory. The solid ellipse represents the positions at downstroke stage while the dashed ellipse represents positions at upstroke stage. XOY is the world coordinate system while xoy is the local coordinate system with the center point located on the center of the flapping trajectories. A_0, the flapping amplitude; B_0, the horizontal deviation amplitude; c, the chord length; α, the wing attack angle regarding the angle between the wing chord and the horizontal plane; β, the flapping plane angle regarding the angle between the wing rotation trajectory and the horizontal plane. (b) The ellipse flapping trajectory. (c) The figure-eight flapping trajectory. (d) The double-figure-eight flapping trajectory.

We study the effects of B_0 and f_1 on the dragonfly flight aerodynamics. $B_0 = 0$ stands for the straight-line flapping with the same motion function as that in ref. [9] (Fig. 2(a)). Different flapping trajectories occur with different f_1 if $B_0 \neq 0$: the ellipse flapping trajectory with $f_1 = f_0$ (Fig. 2(b)), the figure-eight flapping with $f_1 = 2f_0$ (Fig. 2(c)), the double-figure-eight flapping with $f_1 = 3f_0$ (Fig. 2(d)). The air density ρ is 1.225 kg/m^3. The air viscosity is set at $\mu=2.45\times10^{-4}$ Pa • s which is larger than the real air value in order to lower the air Reynolds number, thus making it possible to perform comparisons with those of Wang [9]. The Reynolds number is 157 (Re=$V_{\max}\times c/v$=157) with $V_{\max}$ as the maximum flapping velocity.

2 The governing equations and boundary conditions

2.1 Governing equations

In the present paper, the following mass and momentum equations are used to simulate the two- dimensional unsteady external laminar flow:

$$\frac{\partial u}{\partial X} + \frac{\partial v}{\partial Y} = 0, \tag{4}$$

$$\frac{\partial u}{\partial t} + u\frac{\partial u}{\partial X} + v\frac{\partial u}{\partial Y} = -\frac{1}{\rho}\frac{\partial p}{\partial X} + v\left(\frac{\partial^2 u}{\partial^2 X} + \frac{\partial^2 u}{\partial^2 Y}\right), \tag{5}$$

$$\frac{\partial v}{\partial t} + u\frac{\partial v}{\partial X} + v\frac{\partial v}{\partial Y} = -\frac{1}{\rho}\frac{\partial p}{\partial Y} + v\left(\frac{\partial^2 v}{\partial^2 X} + \frac{\partial^2 v}{\partial^2 Y}\right). \tag{6}$$

Because the wing has different positions versus time, the computational domain and the unit control volume have to be changed periodically. Therefore, the computational domain has to be re-plotted at each time step. To keep conservation, in eqs. (4)−(6) the dynamic grid effect should be taken into account. Considering the grid moving velocity of V_g, the mass and momentum equations are written in the form of the integrated governing equations

$$\frac{d}{dt}\int_\Omega \rho d\Omega + \int_{\partial\Omega}\rho(V - V_g)\cdot dA = 0, \tag{7}$$

$$\frac{d}{dt}\int_\Omega \rho u d\Omega + \int_{\partial\Omega}\rho u(V - V_g)\cdot dA$$
$$= \int_{\partial\Omega}\mu\nabla u\cdot dA + \int_\Omega\left(-\frac{\partial p}{\partial X}\right)d\Omega, \tag{8}$$

$$\frac{d}{dt}\int_\Omega \rho v d\Omega + \int_{\partial\Omega}\rho v(V - V_g)\cdot dA$$
$$= \int_{\partial\Omega}\mu\nabla v\cdot dA + \int_\Omega\left(-\frac{\partial p}{\partial Y}\right)d\Omega. \tag{9}$$

The conservative integrated governing equation for any scalar quantity ϕ is written as

$$\frac{d}{dt}\int_\Omega \rho\phi d\Omega + \int_{\partial\Omega}\rho\phi(V - V_g)\cdot dA$$
$$= \int_{\partial\Omega}\mu\nabla\phi\cdot dA + \int_\Omega S_\phi d\Omega, \tag{10}$$

where Ω is the control volume with the moving boundary, and $\partial\Omega$ is the boundary of the control volume. Eq. (10) becomes the mass conservation equation when $\phi = 1$ and the momentum equations when $\phi = u$ and $\phi = v$.

The grids are to be re-plotted at each new time step. Once the grids at the n time step and the newly designed grids at the $n+1$ time step are known, we have the grid moving velocity $\overline{V}_g$ and Ω^n as well as Ω^{n+1} over the entire computational domain. The parameters at the previous n time step located in the grids of the $n+1$ time step can be interpolated via the values at the n time step. Thus the variable control volume problem of the first order backwind difference term for the partial differential term versus time and the moving velocity of the dynamic grids encountered in the convective term in eq. (10) can be written as

$$\frac{d}{dt}\int_{\Omega}\rho\phi d\Omega = \frac{(\rho\phi\Omega)^{n+1} - (\rho\phi\Omega)^n}{\Delta t}. \qquad (11)$$

Thus for the present two-dimensional wing flapping motion, one mass and two momentum equations consisting of three unknown variables (u, v, p) are closed, which can be solved under the given initial and boundary conditions.

2.2 The initial and boundary conditions

Fig. 3 shows the computational domain with the wing as the internal boundary of the flow field. The dynamic velocity of the internal wall boundary can be obtained by differentiating eqs. (1)－(3) and decomposed on the X and Y coordinates into

$$u(t) = -A_0\pi f_0\sin(2\pi f_0 t)\cos\beta - B_0\pi f_1\cos(2\pi f_1 t)\sin\beta, \qquad (12)$$

$$v(t) = -A_0\pi f_0\sin(2\pi f_0 t)\sin\beta + B_0\pi f_1\cos(2\pi f_1 t)\cos\beta, \qquad (13)$$

$$\omega(t) = \frac{\pi}{2}\pi f_0\cos(2\pi f_0 t + \varphi). \qquad (14)$$

Eqs. (12)－(14) are the internal boundary conditions over the computational domain. The external boundary condition is set as the zero pressure reference to the environment pressure. The initial internal boundary condition can be obtained by setting eqs. (12)－(14) at $t = 0$ as

$$u(0) = -B_0\pi f_1\sin\beta, \qquad (15)$$

$$v(0) = B_0\pi f_1\cos\beta, \qquad (16)$$

$$\omega(0) = \frac{\pi}{2}\pi f_0\cos\varphi. \qquad (17)$$

Velocities are set at zero except on the internal wing boundary. The initial pressure is zero relative to the environment pressure. Eq. (10) is solved using SIMPLEC, second order up-wind numerical scheme.
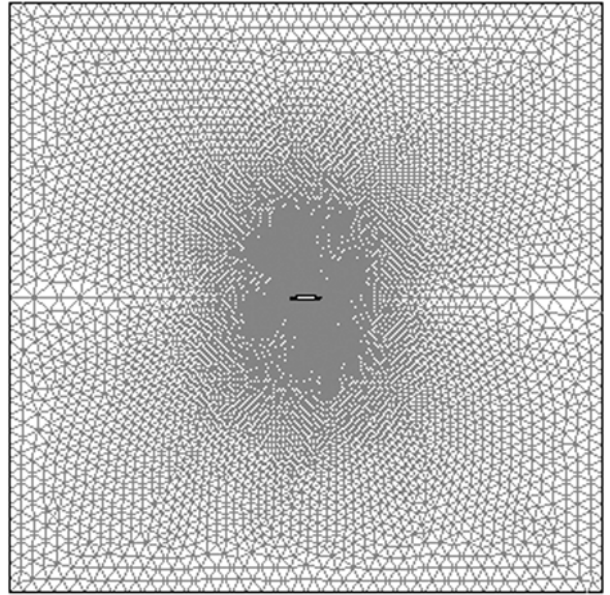

Fig. 3.   The grid structure over the entire computational domain.

3   Results and discussion

3.1   Validation of the numerical simulation

Theoretically, the external boundaries should be infinitely far away from the flapping wing for the present external flow field problem. However, a real CFD modeling only considers a limited computational domain. Several computational domain sizes are used with its length of $5c$, $10c$ and $15c$ to identify the size effect on the flight aerodynamics. It is shown that the CFD modeling results are not affected by the computational domain size as long as its length is larger than $10c$.

Another issue is the grid quality. A preferred non-uniform grid system can be obtained by choosing suitable grid re-plotting parameters. Thus denser populated grids are arranged near the wing boundary and coarser grids are arranged far way from the wing (Fig. 3). In such a way we can not only obtain the flow field, but also save the computation time. A gradual change in the control volume versus time during the grid regeneration process for a successive of time steps is ensured;

thus the numerical simulation is stable. Totally 40000 triangle grids are used over the entire computational domain. The use of the triangular grids is helpful for the grid re-plotting purpose (Fig. 3).

In order to demonstrate the feasibility of the present numerical simulation, the computation results are compared with those of Wang[9] for a similar run case. The wing thickness to the chord ratio is not given in ref. [9] but it is set at 1/8. The lift/drag force coefficients attain the steady periodic variation after more than ten flapping cycles and the computation is stopped there. Fig. 4 shows very similar parameter trends of the lift/drag force coefficients versus time with only slight differences in the amplitudes for the present computations and those of Wang[9], which may be due to the different wing thicknesses to the chord ratio used in the two simulations. The lift force is the Y (vertical) component of the composition of forces with positive Y coordinate, while the drag force is the X component of the composition of forces with positive X coordinate (Fig. 4). The negative drag force is actually the thrust force. For instance, the insect has the net thrust force if the average drag force over a flapping cycle period is negative for a fore flight insect. Assume that the ellipse wingspan is 5 cm and the wing width is 1 cm, the average lift force for the two pairs of wings is 0.0053 N using the computed average lift and drag forces over unit wingspan length of 0.034 N/m and 0.018 N/m, respectively. Then the average lift force is larger than a typical dragonfly weight, which should be in the range

of $0.001 - 0.0025$ N[9,20−23]. Thus the dragonfly can not only perform the normal flight but also has the maneuver performance. These results validate the correct and reasonable trends of the present numerical simulations.

For simplicity, the coefficients of lift/drag force, thrust force, and torque are defined as

$$C_L = \frac{Lift}{0.5\rho\overline{V}^2 c}, \quad C_D = \frac{Drag}{0.5\rho\overline{V}^2 c},$$

$$C_T = \frac{Thrust}{0.5\rho\overline{V}^2 c} = -C_D, \quad C_M = \frac{Moment}{0.5\rho\overline{V}^2 c^2} \quad (18)$$

where $\overline{V}$ is the average flapping velocity over a flapping cycle period, $\overline{V} = 2f_0 A_0$.

3.2 Effect of different flapping trajectories

Some authors have dealt with the translational flapping trajectory for the insect aerodynamics without considering the horizontal deviation effect on the lift/drag force coefficients. However, the horizontal deviation indeed exists for the real insect flight[6,21,24]. In the present paper, based on the flapping frequency of the horizontal deviation, the wing flapping trajectories are divided into three groups: the ellipse, the figure-eight, and the double-figure-eight flapping (see sec. 3.1 below). Generally insects have thin wings with the wing thickness-to-chord ratio being 1/20 and the phase difference of $\varphi = 0$ for the dragonfly species.

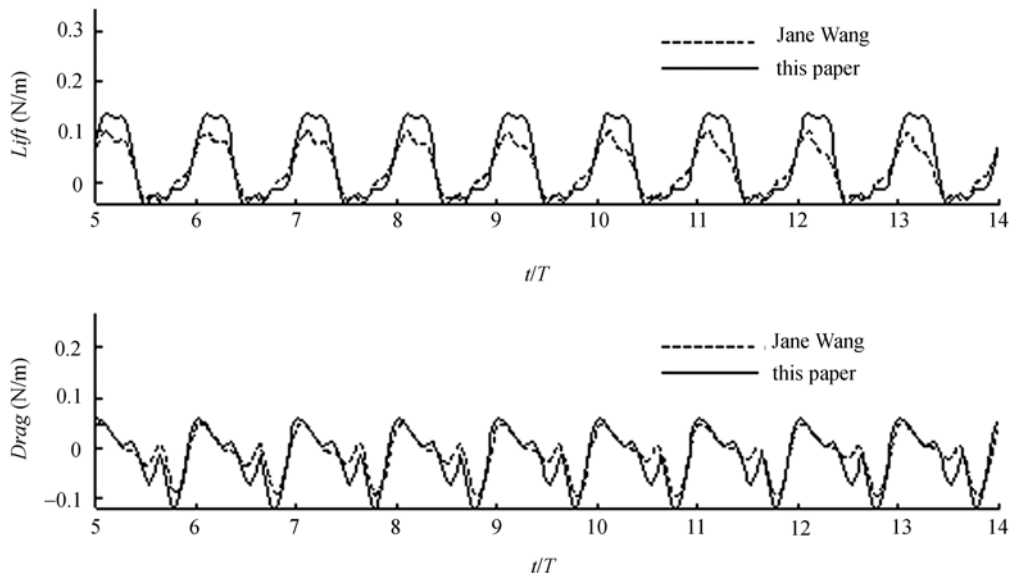The lift and drag force coefficients have the following common characteristics: the lift forces are mainly

Fig. 4. Comparisons of the present computed lift/drag coefficients with those of ref. [9]. The wing flapping cycle period T=0.025 s.
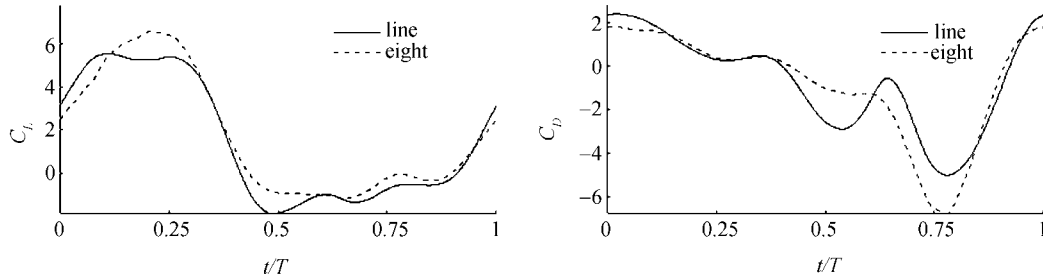
Fig.5. Comparisons of the lift/drag, torque coefficients for the translational and figure-eight flapping trajectories with the horizontal deviation of $A_0/10$.

provided during the wing downstroke and the drag forces are mainly coming from the wing upstroke (Fig. 5 only illustrates the lift/drag force coefficients for the translational and figure-eight flapping trajectories). At the initial flapping position, the lift force coefficients are sharply increased, which is well consistent with the experimental measurements by Sane and Dickinson[6]. The maximum lift force coefficients are all beyond 5 for the four flapping trajectories. They are even larger than 6 for the figure-eight and double-figure-eight flapping trajectories, sufficiently larger than unity under the steady flight status.

The lift/drag force coefficients are analyzed via comparisons of the figure-eight and the translational flapping trajectories. Fig. 5 shows that the larger average lift force coefficient is contributed by the higher dynamic value at the time $t=0.25T$ and $t=0.50T$ while the higher average thrust force coefficient is contributed by the higher dynamic value at the time $t=0.75T$ for the figure-eight flapping trajectory than those for the translational one. For the figure-eight flapping motion, the wing is located at the center point during the downstroke flapping at $t=0.25T$. The vortices at the top surface of the wing leading-edge and trail-edge are larger for the figure-eight flapping motion than those for the translational one (Fig. 6(c)-1, 2), while the vortices are moving toward the wing trail-edge for the translational flapping mode. These effects cause the larger pressure difference between the top and bottom of the wing surfaces, leading to higher lift forces for the figure-eight flapping motion than those for the translational one (Fig. 6(c)-3,4). At this time, there exists smaller drag force difference for the two flapping motions, which is caused by the nearly zero X component of the composition of forces. From the kinematics point of view, there is an additional horizontal deviation velocity leading to the nearly vertical downward direction of the velocity vector (Fig. 7, $t=0.25T$) for the figure-eight flapping motion. Meanwhile, the velocity-induced drag force approaches the vertical upward direction, leading to the higher lift force. At $t=0.5T$, there is an additional horizontal deviation velocity along the Y coordinate in the xoy plane, which decreases the damping effect of the wing leading-edge on the leading-edge and trail-edge vortices of the top wing surface, leading to larger rotation velocity of the vortices and enlarged low pressure area (Fig. 6(e)-3,4). Thus the lift/drag force coefficients are higher for the figure-eight flapping motion than the translational one. At $t=0.75T$, the wing is located at the center point of the upstroke flapping, the wing has higher pressure region on the up-edge (the right side of the wing, as shown in Fig. 6(g)-4), leading to the larger pressure area, hence larger fore thrust force for the figure-eight flapping motion than that for the translational one. At this time, there is a small lift force difference due to the vertical position of the wing. The Y component of the composition of forces approaches zero.

Whether for the translation or figure-eight flapping trajectories, the leading-edge vortex is attached to the wing surface, leading to the maintained low pressure on the top wing surface (Fig. 8). This is one of the high lift force mechanisms[7,12]. Fig. 8 shows that the detachment of the leading-edge and trail-edge vortices is induced by the fast wing rotation with its direction inverse to the flapping velocity. The detachment of the vortices for various flapping modes has the same frequencies. The detachment of a pair of vortices corresponds to a flapping cycle. Fig. 8 shows the vortex streets for the straight-line and figure-eight flapping modes. The vortex street is slightly stronger for the figure-eight than that for the straight-line flapping mode. Considering the insect and the gas as a single system, according to the momentum conservation principle, the higher the air flow rate and the larger velocity of the gas flowing downward, the larger the lift forces will be. Therefore, the lift/drag force coefficients are larger for
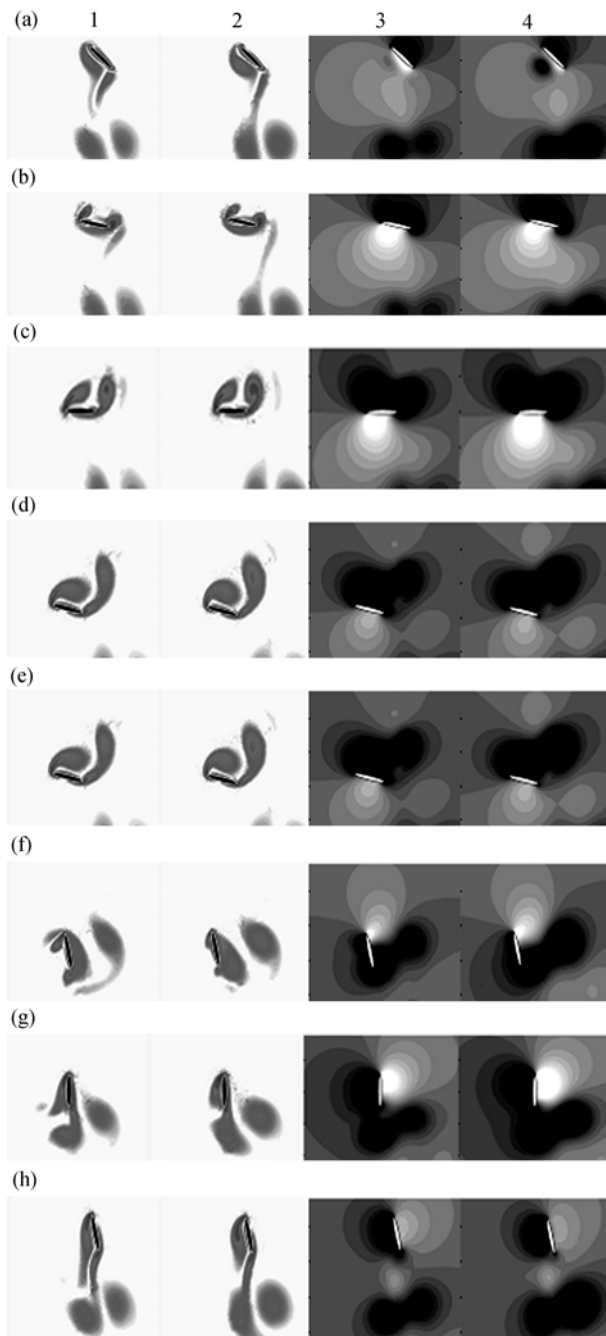
Fig. 6. Comparisons of the vortices and pressure counters for the translational and figure-eight flapping trajectories. The first and second columns are the vortices for the translational and figure-eight flapping trajectories, respectively. The third and fourth columns are the pressure counters for the translational and figure-eight flapping trajectories. The white color represents the high pressure while the black represents the low pressure. (a) t=0.0T (t=1.0T); (b) t=0.125T; (c) t=0.25T; (d) t=0.375T; (e) t=0.5T; (f) t=0.625T; (g) t=0.75T; (h) t=0.875T.

the figure-eight than those for the straight-line flapping mode. The vortices are detached in the direction of the

right-downward. Thus, the compositions of the forces are in the direction of left-upward.
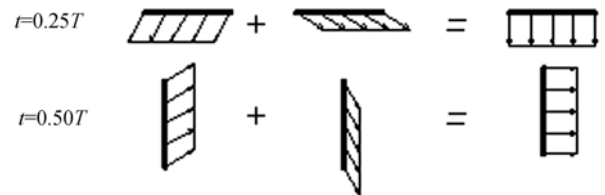

Fig. 7. The velocity composition at t=0.25T and t=0.50T for the figure-eight flapping motion of the wing.
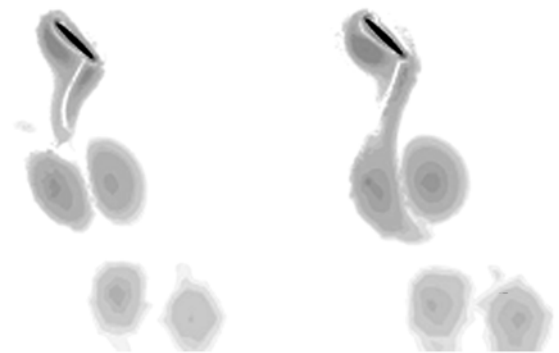

Fig. 8. The vortex streets for the translational (left subfigure) and the figure-eight flapping trajectories (right subfigure).

Table 1 lists the average lift/drag coefficients over a full cycle for the ellipse, figure-eight and the double-figure-eight flapping trajectories for comparison with the available experimental measurements. With the horizontal deviation $B_0 = A_0/10$, the average lift force coefficient is increased by 24% and 76% for the ellipse flapping trajectory and the figure-eight flapping mode respectively, in comparison with the maximum lift coefficient under the steady flight motion. Among the three flapping modes shown in Table 1, the average lift force coefficients are smaller for the ellipse and double-figure-eight flapping modes than those for the figure-eight flapping mode. Meanwhile the average lift and drag force coefficients are greater for the figure-eight flapping mode than those for the straight-line one. For the ellipse flapping mode, the lift force coefficient is decreased with the increasing horizontal deviation, which is well consistent with the experimental measurements by Sane and Dickinson[6].

As shown in Table1, the loft/drag force coefficients are increased and then decreased with the continuous increasing horizontal deviation, which is not consistent with the results of Sane and Dickinson[6]. Ref. [6] indicated that the lift/drag force coefficients are de-

creased with the increasing horizontal deviation for the figure-eight flapping trajectory. The above inconsistency maybe due to the use of different horizontal deviation parameters. In the present paper, $B_0=A_0/10$ and $B_0=A_0/5$ with the deviation angles less than 5°, while large horizontal deviations were used in Sane and Dickinson[6]. The experimental measurements also cannot mach the predictions by the quasi-steady model. This is because the quasi-steady theory cannot describe the flight aerodynamics with the figure-eight flapping trajectory.

Table 1　The average lift/drag force coefficients for different flapping trajectories ($B_0=0$ represents no horizontal deviation motion, i.e. the translational flapping motion)

		$B_0=0.0$	$B_0=A_0/10$	$B_0=A_0/5$
Ellipse	C_L	1.46	1.24	0.98
	C_D	−0.75	−0.93	−0.99
	C_R	**1.65**	**1.55**	**1.40**
Figure-eight	C_L	1.46	1.76	1.55
	C_D	−0.75	−0.88	−0.87
	C_R	**1.65**	**1.97**	**1.77**
Double-figure-eight	C_L	1.46	1.43	1.11
	C_D	−0.75	−0.79	−0.70
	C_R	**1.65**	**1.64**	**1.32**

4　Conclusions

Via the present numerical simulations it is found that the insect lift/drag force coefficients are greatly influenced by the flapping trajectories. By analyzing the ellipse, straight-line, figure-eight and double-figure-eight flapping trajectories, the maximum lift force coefficients are shown to exceed five, which are sufficiently larger than unity under the steady state flight condition. The ellipse and double-figure-eight flapping trajectories causes the lift force to be lower than the translational flapping one. The present study of the flapping trajectories on the insect aerodynamics is helpful for the design of the Micro-air-vehicles (MAVs).

References

1. Grodnitsky, D. L., Morozov, P. P., Vortex formation during tethered flight of functionally and morphologically two-winged insects, including evolutionary considerations on insect flight, J. Exp. Bio., 1993, 182: 11－40.
2. Dickinson, M. H., Götz, K. G., The wake dynamics and flight forces of the fruit fly *Drosophila melanogaster*, J. Exp. Bio., 1996, 199: 2085－2104.
3. Dickinson, M. H., Götz, K. G., Unsteady aerodynamic performance of model wings at low Reynolds numbers, J. Exp. Bio., 1993, 174: 45－64.
4. Ellington, C. P., Berg, C. V. D., Willmott, A. P. et al., Leading-edge vortices in insect fligh, Nature, 1996, 384: 626－630. [DOI]
5. Dickinson, M. H., Lehmann, F. O., Sane, S. P., Wing rotation and the aerodynamic basis of insect flight, Science, 1999, 284: 1954－1960. [DOI]
6. Sane, S. P., Dickinson, M. H., The control of flight force by a flapping wing: Lift and drag production, J. Exp. Bio., 2001, 204: 2607－2626.
7. Birch, J. M., Dickinson, M. H., Spanwise flow and the attachment of the leading-edge vortex on insect wings, Nature, 2001, 412: 729－733. [DOI]
8. Liu, H., Ellington, C. P., Kawachi, K. et al., A computational fluid dynamic study of hawkmoth hovering, J. Exp. Bio., 1998, 201: 461－477.
9. Wang, Z. J., Two dimensional mechanism for insect hovering, Physical Review Letters, 2000, 85: 2216－2219. [DOI]
10. Wang, Z. J., Birch, J. M., Dickinson, M. H., Unsteady forces and flows in low Reynolds number hovering flight: Two-dimensional computations vs robotic wing experiments, J. Exp. Bio., 2004, 207: 449－460. [DOI]
11. Lan, S. L., Sun, M., Aerodynamic force and flow structure of two airfoils in flapping motions, Acta Mechanica Sinica, 2001, 17: 310－331.
12. Sun, M., Tang, J., Unsteady aerodynamic force generation by a model fruit fly wing in flapping motion, J. Exp. Bio., 2002, 205: 55－70.
13. Ho, S., Nassef, H., Pornsinsirirak, N., Tai, Y. C. et al., Unsteady aerodynamics and flow control for flapping wing flyers, Progress in Aerospace Science, 2003, 39: 635－681. [DOI]
14. Ellington, C. P., The aerodynamic basis of insect flight I-V, Phil. Trans. R. Soc. Lond. B, 1984, 305: 1－181.
15. Zanker, J. M., Gotz, K. G., The wing beat of Drosophila melanogaster II.dynamics, Phil. Trans. R. Soc. Lond. B, 1990, 327: 19－44.
16. Fry, S. N., Sayaman, R, Dickinson, M H., The aerodynamics of free-flight Maneuvers in *Drosophil*, Science, 2003, 300: 495－498. [DOI]
17. Wang, Z. J., The role of drag in insect hovering, J. Exp. Bio., 2004, 207: 4147－4155. [DOI]
18. Ramamurti, R., Sandberg, W., Computational study of 3-D flapping foil flows, AIAA-2001-0605.
19. Togashi, F., Ito, Y., Murayama, M., Nakahashi, K. et al., Flow simulation of flapping wings of an insect using overset unstructured grid, AIAA-2001-2619.
20. Okamoto, M., Yasuda, K., Azuma, A., Aerodynamic characteristics of the wings and body of a dragonfly, J. Exp. Bio., 1996, 199: 281－294.
21. Wakeling, J., M,Ellington, C. P., Dragonfly flight Ⅰ: Gliding flight and steady-state aerodynamic forces, J. Exp. Bio., 1997, 200: 543－556.
22. Wakeling, J. M., Ellington, C. P., Dragonfly flight Ⅱ: Velocities, accelerations and kinematics of flapping flight, J. Exp. Bio., 1997, 200: 557－582.
23. Wakeling, J. M., Ellington, C. P., Dragonfly flight Ⅲ: Lift and power requirements, J. Exp. Bio., 1997, 200: 583－600.
24. Weis-Fogh, T., An exception is a special class of tiny insects, J. Exp. Bio., 1973, 59:169－230.